Title

Automated unsupervised multi-parametric classification of adipose tissue depots in skeletal muscle

Journal

Journal of Magnetic Resonance Imaging, 37(4)

ISSN

1053-1807

Authors

Valentinitsch, Alexander
Karampinos, Dimitrios C
Alizai, Hamza
et al.

Publication Date

2013-04-01

DOI

10.1002/jmri.23884

Peer reviewed

Published in final edited form as:
J Magn Reson Imaging. 2013 April ; 37(4): 917–927. doi:10.1002/jmri.23884.

Automated unsupervised multi-parametric classification of adipose tissue depots in skeletal muscle

Alexander Valentinitsch, MS[1,2], **Dimitrios C. Karampinos, PhD**[1], **Hamza Alizai, MD**[1], **Karupppasamy Subburaj, PhD**[1], **Deepak Kumar, PhD**[1], **Thomas M. Link, PhD**[1], and **Sharmila Majumdar, PhD**[1]

[1]Department of Radiology and Biomedical Imaging, University of California, San Francisco, San Francisco, CA, USA

[2]Computational Image Analysis and Radiology Lab, Department of Radiology, Medical University of Vienna, Vienna, AUSTRIA

Abstract

Purpose—To introduce and validate an automated unsupervised multi-parametric method for segmentation of the subcutaneous fat and muscle regions in order to determine subcutaneous adipose tissue (SAT) and intermuscular adipose tissue (IMAT) areas based on data from a quantitative chemical shift-based water-fat separation approach.

Materials and Methods—Unsupervised standard k-means clustering was employed to define sets of similar features (k = 2) within the whole multi-modal image after the water-fat separation. The automated image processing chain was composed of three primary stages including tissue, muscle and bone region segmentation. The algorithm was applied on calf and thigh datasets to compute SAT and IMAT areas and was compared to a manual segmentation.

Results—The IMAT area using the automatic segmentation had excellent agreement with the IMAT area using the manual segmentation for all the cases in the thigh (R^2: 0.96) and for cases with up to moderate IMAT area in the calf (R^2: 0.92). The group with the highest grade of muscle fat infiltration in the calf had the highest error in the inner SAT contour calculation.

Conclusion—The proposed multi-parametric segmentation approach combined with quantitative water-fat imaging provides an accurate and reliable method for an automated calculation of the SAT and IMAT areas reducing considerably the total post-processing time.

Keywords

magnetic resonance imaging (MRI); water-fat imaging; subcutaneous adipose tissue (SAT); intermuscular adipose tissue (IMAT); fat quantification; multi-parametric clustering

INTRODUCTION

Metabolic abnormalities including obesity and type 2-diabetes have been associated with alterations in the volume and the regional distribution of adipose tissue in different body parts, including abdominal and skeletal muscle regions (1,2). Specifically, metabolic diseases have been linked with an increase in the volume of the visceral adipose tissue (VAT) (3), which constitutes the fat between abdominal organs, and with an increase in the volume of the intermuscular adipose tissue (IMAT) (4–6), which is composed of the fat

Corresponding Author Address: Alexander Valentinitsch, Währinger Gürtel 18-20, A-1090 Wien, Tel.: +43 1 40400 – 5843, Fax: +43 1 40 400 - 4898, alexander.valentinitsch@meduniwien.ac.at.

located between the muscle fiber bundles and beneath the muscle fascia. The subcutaneous adipose tissue (SAT) compartment, consisting of fat located directly beneath the skin, is usually considered as a metabolically-different fat depot than the VAT and IMAT compartments, especially in the context of type 2 diabetes (5).

Magnetic Resonance Imaging (MRI) constitutes a powerful non-invasive imaging tool for determining adipose tissue volume and regional distribution in both cross-sectional and longitudinal studies (7–9). An MRI-based characterization of the body fat depots, in general, requires: (a) a robust fat quantification, and (b) a reproducible extraction of subcutaneous fat, abdominal and skeletal muscle regions, in order to determine the volume of SAT, VAT and IMAT respectively. The extraction of the volume of the different fat depots has been traditionally accomplished using T_1-weighted imaging. Although sensitive to coil profile effects, T_1-weighted imaging is a simple and reliable technique for investigating large fat depots (7,8). However, it needs to be combined with effective segmentation approaches in order to separate adipose tissue from non-adipose tissue, especially in the presence of strong partial volume effects while investigating small fat depots like the VAT and IMAT compartments (10,11). More recently T_1-weighted imaging has been combined with water suppression (12,13) and with dual acquisitions using water suppression and fat suppression (14) for the development of clustering image-processing approaches to automatically segment the adipose tissue into different compartments.

Chemical shift-based water-fat separation approaches, like multi-point Dixon methods (15,16) and the iterative decomposition of water and fat with echo asymmetry and least-squares estimation (IDEAL) method (17,18), have been recently applied to measure a quantitative proton density fat fraction map in different body parts. These techniques have two important advantages compared to T_1-weighted imaging. First, chemical shift-based water-fat separation techniques can inherently differentiate adipose tissue from non-adipose tissue by computing fat area based on fat fraction maps that are inherently insensitive to coil profile effects. Therefore, chemical shift-based water-fat separation techniques are ideal for measuring the area of small fat depots in the presence of strong partial volume effects (19). Second, the inherent multi-modal imaging (MMI) property of chemical shift-based water-fat separation makes it an ideal candidate for multi-parametric segmentation of the different adipose tissue compartments, as has been previously proposed in dual T_1-weighted acquisitions using water suppression and fat suppression (14).

Recent studies employing water-fat imaging techniques have suggested approaches for automated classification of adipose tissue depots in the abdominal regions for differentiating between SAT and VAT (20,21). To the best of our knowledge, there has been no previous study employing a multi-parametric segmentation technique on data acquired using a quantitative chemical shift-based water-fat separation approach for differentiating between SAT and IMAT. Defining tissue depots (i.e. manually and semi-automatically) is usually time consuming and there is need for a faster automated algorithm. An automated, accurate and reproducible segmentation technique for identifying the SAT and the muscle region can be technically challenging due to severe muscle fatty infiltration and strong increase of intermuscular fat in numerous pathologic conditions (22).

The purpose of the present study is (a) to develop an automated unsupervised multi-parametric segmentation method of the SAT and muscle region to determine SAT and IMAT areas based on the images from a quantitative chemical shift-based water-fat separation approach and (b) to validate the developed methodology in two different subject groups, one including the calf muscles of postmenopausal female subjects with and without diabetes and one including the thigh muscles of older subjects with and without knee osteoarthritis.

MATERIALS AND METHODS

Subjects

The present study included data from the MR images of calf muscles of 28 female subjects (age: 65.0 ± 5.8, BMI: 27.5 ± 4.2) and the thigh muscle of 20 subjects (age: 56.5 ± 8.5, BMI: 23.8 ± 5.6). The subjects included in the present study are derived from two separate patient studies. The calf muscle images were obtained from subjects enrolled in a study aiming to investigate differences in the regional distribution of skeletal muscle adipose tissue in postmenopausal women with type-2 diabetes compared to healthy controls (19). Inclusion criteria were defined as postmenopausal status, age between 50–75 years, body mass index (BMI) 18–37 kg/m^2, and the ability to walk without assistance. The thigh muscle dataset is from a cohort of older subjects (> 35 years), with (Kellgren-Lawrence grade = 2, 3 or 4, symptomatic) and without (Kellgren-Lawrence grade = 0 or 1, no knee pain) knee osteoarthritis to investigate the relationship between the longitudinal changes in the morphology and composition of knee articular and meniscal cartilage, trabecular bone and thigh muscles (23–26). Subjects were excluded from either study if they had contra-indications to MR scanning. Both studies were approved by the local Institutional Review Board and conducted in accordance with the Committee for Human Research. All subjects gave written informed consent prior to participation in the two studies.

16 subjects with type-2 diabetes and 12 without were included for the evaluation of the performance of the developed method in the calf. Additionally, 7 subjects with knee osteoarthritis and 17 without were used for the evaluation of the method performance in the thigh.

MRI measurements

The right middle-calf muscle region of the first group (elderly postmenopausal women) and the distal thigh muscle region (area 14 cms proximal to superior pole of patella) of the second patient group (adults with and without knee osteoarthritis) were scanned on a 3.0 T Signa HDx scanner (General Electric Healthcare, Waukesha, WI) using an 8-channel low extremity coil with an investigational version of a 3D six-echo spoiled gradient echo (SPGR) sequence with a mono-polar gradient readout. The SPGR sequence acquired six echoes in three repetitions (with two echoes per repetition time) with two fly-back readouts, and echo spacing selected to avoid water-fat phase shifts of 0 or 2π. The parameters of the calf acquisition included: TR/TE/ΔTE=12/1.4/0.7 ms, flip angle=3°, bandwidth=83.33 kHz, 180×180 matrix size, FOV=18 cm, 30 slices with 4 mm thickness. The parameters of the thigh acquisition included: TR/TE/ΔTE=10.8/1.3/0.7 ms, flip angle=3°, bandwidth=83.33 kHz, 180×180 matrix size, FOV=20 cm, 28 slices with 5 mm thickness. The acquisition time was 3 min and 45 s for the calf scan and 3 min and 7 s for the thigh scan.

The multi-echo SPGR images were reconstructed using an online version of the IDEAL technique employing a region growing algorithm for the fieldmap estimation to avoid water-fat swaps (27). The separation of water and fat signal was based on the IDEAL algorithm (18) with a multi-peak fat spectrum model and single T_2* correction (28), using the precalibrated fat spectrum as in (29). A six-echo acquisition was employed as reconstructions of six-echo data have been previously frequently used in single T_2*-corrected water-fat separation and have been shown to be not affected by the susceptibility-induced fat resonance shift effect in skeletal muscle (30). In-phase images were calculated by taking the sum of the separated water and fat images. Out-of-phase images were also calculated by taking the absolute value of the difference of the separated water and fat images. Fat fraction images were generated by computing the ratio of the separated fat signal over the sum of the separated water and fat signals. A 3° flip angle was used to

minimize the bias on the fat fraction induced by the large T_1 difference between water and fat in skeletal muscle (31–33). A hybrid approach combining magnitude and complex fitting was used to compensate for eddy current effects, as proposed by Yu et al. (34).

Automatic segmentation algorithm

The algorithm developed for the segmentation of the muscle and fat depot compartments in order to quantify SAT and IMAT areas was based on the same multi-parametric clustering approach for both calf and thigh datasets, using the multi-modal images derived after the water-fat separation step. Unsupervised standard k-means clustering was employed to define sets of similar features (k = 2) within the whole multi-modal image. Water, fat and in-phase images composed the multi-modal volume, provided as input to the algorithm. All the images (e.g. water, fat, and in-phase images) were first preprocessed by applying a Gaussian smoothing operator (sigma = 0.3, Gaussian kernel = 1.2). Additionally, a median filter (which is a nonlinear filter) was applied on the in-phase images. The automated image processing chain was composed of three primary stages. The different steps of the three segmentation stages are schematically shown in Figure 1 and described in detail below. Every stage resulted in a different binarization step of the image. In the first stage (tissue region segmentation), the whole tissue was segmented by clustering the distribution of three different diagnostic images (in-phase, water and fat images) to extract the outer contour of the SAT region. In the second stage (muscle region segmentation), the muscle region was determined by clustering on the tissue region (masked from stage 1) using water and fat images to extract the inner contour of the SAT region. In the third stage (bone region segmentation), the bones were identified and distinguished from the muscle region. The bone identification stage was split into two substages. In order to stabilize the performance of the algorithm in cases with thin cortical bone, the bone marrow was first extracted, using the same features as the ones used for clustering on the masked compartment in stage 1. The cortical bone was next identified, using a threshold, defined as local minimum between the smallest and highest peak of the histogram. In the thigh segmentation process, the cortical bone of the femur has in general high thickness and the first step of the bone segmentation stage was therefore not necessary. The combination of all stages resulted in the extraction of SAT and muscle regions, which could be used to compute SAT and IMAT areas respectively.

Stage 1: Tissue region segmentation—At first the tissue and the background phase in the image were discretized using a multi-parametric clustering method based on three different intensity values (in-phase, water and fat) (step 1a). To identify the outer contour of the SAT region 2D morphological closing (3 pixels, equivalent to 2.1 mm) was performed on the binary image to close all perforations (i.e. vessels and small bones) in the muscle (step 1b). The residual void (i.e femoral or tibial bone) in the muscle was removed using 2D connectivity criterion to select the single largest mutually connected object to fill the tissue (step 1c). The result of stage 1 was a mask of the specific tissue (i.e. calf or thigh) (mask A in Fig. 1).

Stage 2: Muscle region segmentation—The boundary between the SAT and the muscle region for IMAT calculation was identified by first clustering only in the masked tissue region with two different intensity values (fat and water) (step 2a). Then a 2D morphological opening (2 pixels, equivalent to 1.4 mm) was performed to remove primarily the skin tissue (i.e. dermis and epidermis combined) (step 2b). A 2D morphological closing was then performed with scaling depending on the selected tissue (calf: 5 pixels, equivalent to 3.5 mm; thigh: 20 pixels, equivalent to 14 mm) (step 2c). Again the residual void (i.e. fibula) was filled by using a set of background pixels that cannot be reached by filling in the

background from the boundary of the muscle (step 2d). The result of stage 2 was a mask of the muscle region (mask B in Fig. 1).

Stage 3: Bone region segmentation—Given the underlying anatomy in the calf, the extraction of two bones was necessary (fibula and tibia). In order to improve the performance of the method in slices with thin cortical bone, the bone segmentation process had to be split into two substages. In the first substage, the bone marrow of either the fibula or tibia was classified using multi-parametric clustering of three different intensity values (in-phase, water and fat) (step 3a). After imposing the mask of the muscle region, 2D morphological opening was performed to remove small voids (2 pixels, equivalent to 1.4 mm), so that only the bone marrow remained in the binary image (step 3b). In the second substage, the cortical bone was removed by thresholding the in-phase image (step 3a*). The threshold was calculated by finding the local minimum between the first peak (assumed to be the black appearance in the image) and the proximate high peak (assumed to be the dark gray area in the image) in the histogram. The thresholded image was then inverted and the inverted image was masked with the specific tissue volume of interest (i.e. calf) to leave only the cortical bone voxels (step 3b*). The image resulting from the bone marrow segmentation substage was subtracted from the image resulting from the cortical bone segmentation substage (step 3c). The residual void (i.e bone marrow) in the muscle was removed using 2D connectivity criterion to select the single largest mutually connected object to fill the bone tissue (step 3d). Remaining areas, which were smaller than the identified bones (i.e. tibia, fibula, femur) were removed. Given the underlying anatomy in the thigh, the extraction of only one bone was necessary (femur). Given the relative high thickness of cortical bone in the femur, the bone segmentation was accomplished using the threshold-based approach. The result of stage 3 was a mask of the bone (mask C in Fig. 1).

Figure 2 shows the definition of SAT and IMAT regions based on the combination of the masks from the three segmentation stages (masks A, B and C).

Comparison with manual segmentation

A single slice for each subject from the calf and thigh group was selected and the automatic segmentation algorithm, implemented in MATLAB (Mathworks, Natick, MA, USA) was run to define the aforementioned masks (masks A, B and C). To test the performance of the proposed automated multi-parametric classification, a trained operator was also asked to generate the three masks using manual contouring. The operator manually contoured the outer contour of the SAT area and the bone contour on the in-phase images. The fat-only images were used for manually contouring the inner contour of the SAT area. The result of the manual contouring was considered as the gold standard and used as ground truth (GT) for the validation of the automatic segmentation.

Agreement in contours—The agreement between the masks derived using the automatic and the manual segmentation was assessed using the Dice coefficient (35) for the SAT mask and the muscle masks (mask B) without including the bones (mask C). In general a DC value of 0 would indicate no overlap, whereas a value of 1 would indicate perfect agreement. As a complementary local measure the local contouring error (LCE) for SAT outer contour, SAT inner contour and bone contour was evaluated. The LCE was defined as the mean distance between the closest corresponding pairs of contouring points of the manual contours and contours resulting from the multi-parametric segmentation.

Agreement in fat depots areas (SAT and IMAT)—The SAT area was determined by computing the area of SAT mask derived using both the automatic and manual segmentation. The IMAT area was determined by multiplying the mean fat fraction in the

muscle region mask (excluding cortical bone and bone marrow regions) with the area of the muscle region mask (excluding cortical bone and bone marrow regions), using both the automatic and manual segmentation.

For the calf dataset, the performance of the automatic segmentation compared to the manual segmentation in terms of computing SAT and IMAT areas was evaluated for different degrees of muscle fat infiltration. Specifically, the calf muscle data were grouped according to the presence of fatty infiltration in the medial gastrocnemius muscle (MG) based on a 5-point semi quantitative scale described by Goutallier (36): G0 (normal), G1 (some fatty streaks), G2 (less fat than muscle), G3 (as much fat as muscle), G4 (more fat than muscle). The grading was performed by a trained radiologist (with two years of experience in musculoskeletal radiology) and was based on visual assessment of muscle fat infiltration on T_1-weighted fast-spin echo images (acquired on the same volume as the SPGR calf images) (22). For the thigh dataset, the performance of the automatic segmentation compared to the manual segmentation in terms of computing SAT and IMAT areas was evaluated for all subjects independent of gender or age.

Statistical analysis

A regression analysis was performed in order to study the agreement in SAT and IMAT area using the proposed automatic approach with the SAT and IMAT area using the automatic approach for both datasets (in the calf and the thigh). A two-tailed Student's t-test (significance level $p = 0.05$) was used to detect differences in slopes and intercepts in the study of the relationship for the determined fat depot areas using the automatic and manual approach. In addition, Bland-Altman plots for the fat depot areas using the automatic and manual approach were generated. The PASWStatistics 18.0 software (SPSS, Inc., Chicago, IL, USA) was used for the entire statistical analysis.

RESULTS

Figure 3 highlights the performance of the proposed multi-parametric segmentation algorithm in the calf by showing representative results for the SAT mask (i.e. contours are superimposed on the fat and water image) and the muscle region mask (i.e. contours are superimposed on the water image) in the calf of subjects with different grades of muscle infiltration in the medial gastrocnemius (MG), characterized by the Goutallier grade. Figure 4 highlights the performance of the proposed multi-parametric segmentation algorithm in the thigh by showing representative results for the SAT mask (i.e. contours are superimposed on the fat and water image) and the muscle region mask (i.e. contours are superimposed on the water image) in the thigh of two male and two female subjects with different ages (one younger and one older subject).

In the calf, the group data analysis showed an overall agreement of the SAT and muscle region without including the bone between the proposed automatic method and the ground truth (GT), as expressed by the Dice coefficient (DC), equal to 0.968 ± 0.014 and 0.971 ± 0.016 respectively. Moreover, the accuracy of the SAT region extraction was stable across muscle infiltration patterns up to grade G3, with Dice coefficients 0.968 ± 0.009, 0.970 ± 0.005, 0.972 ± 0.005 and 0.968 ± 0.005 for grades G0, G1, G2 and G3 respectively. Similar accuracy was observed for the extraction of the muscle regions with Dice coefficients 0.974 ± 0.006, 0.975 ± 0.004, 0.977 ± 0.005 and 0.967 ± 0.011 for grades G0, G1, G2 and G3 respectively. The lowest overlap between automatic and manual segmentation was observed, as expected, for the group with the highest muscle infiltration grade in the medial gastrocnemius (MG): the Dice coefficient for the SAT region was 0.956 ± 0.034 and the Dice coefficient for the muscle region without the bones was 0.948 ± 0.036. The calf Dice coefficient results were also consistent with the local contouring error (LCE) results, shown

in Figure 5. The group with the highest grade of fat infiltration in the medial gastrocnemius muscle (G4) had the highest local contouring error for the SAT inner contour, which was equal to 1.4 ± 1.1 pixels. However, all other contours performed below the 1-pixel error mark (Fig. 5).

In the thigh, the group data analysis resulted in an overall Dice coefficient for the segmentation of the SAT region and the muscle region without the bone equal to 0.972 ± 0.008 and 0.979 ± 0.008 respectively. There was no significant difference in the segmentation performance between female and male subjects. The thigh Dice coefficient results were also consistent with the local contouring error (LCE) results, shown in Figure 5. The LCE for the SAT inner contour was 1.1 ± 0.3 pixels (female: 1.2 ± 0.3 pixels, male: 1.1 ± 0.2 pixels). The bone and the SAT outer contour had an LCE below 0.4 pixels (Fig. 5).

Table 1 summarizes linear regression results on the agreement of SAT and IMAT area estimates between the automatic segmentation approach and manual contouring (in the calf and the thigh). Figure 6 shows the regression analysis relationships between the IMAT area computed with the automatic segmentation and the IMAT area computed with the manual segmentation in the calf and the thigh. Figure 7 shows the Bland Altman plots for the assessment of both SAT and IMAT areas by the automatic and manual segmentation in the calf and the thigh.

The slope of the relationship between the SAT area determined with the automatic and the SAT area determined manual segmentation was not statistically significant from unity in both the calf and the thigh (Table 1). The intercept of the relation between the SAT area determined with the automatic and SAT area determined with the manual segmentation was also not statistically significant from zero in both the calf and the thigh (Table 1).

In the calf, the extraction of the IMAT area using the automatic approach had higher agreement with the IMAT area using the manual approach in areas with low and moderate area of IMAT (e.g. IMAT area below 6 cm^2) (Fig. 6). The slope of the relation between the IMAT area determined using the automatic approach and the IMAT area determined using the manual approach differed significantly from the unity (Table 1) due to underestimation of IMAT area using the automatic segmentation in the cases of muscles with severe fat infiltration or high area of IMAT (Fig. 6). By excluding the cases with IMAT area above 6 cm^2 in the regression analysis, the performance increased significantly (R^2: 0.92: slope: 0.924 ± 0.069, intercept: 0.002 ± 0.028) and the slope and intercept were not significantly different from unity and zero respectively. In the thigh, only the intercept of the relationship between the IMAT area determined using the automatic approach and the IMAT area determined using the manual approach differed significantly from zero (Table 1) due to a slight overestimation of IMAT area using the automatic approach and including a small part of subfascial fat into IMAT (Fig. 6).

Figure 8 shows two different extreme cases from the calf dataset where the automatic segmentation overestimated or underestimated the IMAT area (i.e. visible outliers in regression plots in Figure 6). The automatic segmentation in the first subject of Fig. 8 did not perform as expected due to the complete fat infiltration of the medial gastrocnemius muscle. The automatic segmentation in the second subject of Fig. 8 did not perform as expected due to the very thin cortical bone in the tibia.

The manual segmentation of the SAT and muscle regions in a single slice of the calf or the thigh took up to 4 minutes, whereas the automatic segmentation of the SAT and muscle regions of a single slice using the proposed automatic segmentation approach took up to 0.25 seconds (in the present implementation on a MAC Pro: 2 * 2.66 GHz 6-Core with 32 GB memory).

DISCUSSION

A three-stage segmentation method using unsupervised multi-parametric k-means clustering on skeletal muscle data acquired using a chemical-shift based water-fat separation approach was developed in order to compute SAT and IMAT areas. The technique was validated in a range of cases in the calf and thigh muscles of both young and elderly subjects, including fatty degenerated muscles of patients with type 2 diabetes or knee osteoarthritis. The proposed method can achieve a robust and consistent separation of the SAT and muscle region across different degrees of muscle fat infiltration in the calf. Even in the thigh the accuracy of the automatic segmentation in the definition of the contours of SAT and muscle regions was high. From a practical standpoint the proposed multi-parametric segmentation algorithm can be easily reproduced and implemented using standard image analysis tools. Additionally, the calculation of the area of fat depots based on the proton density fat fraction map of the chemical shift-based water-fat separation minimizes the sensitivity of the fat depot extraction (especially for the IMAT) to partial volume effects.

The computation of the volume of the different fat depots involves, in general, two main steps. The first step is related to the extraction of the SAT and muscle regions and the second step is related to the distinction between adipose tissue and non-adipose tissue in voxels with partial volume effects, where both water and fat are present. Different techniques have been proposed in order to accomplish the above two steps, but both steps can, in general, benefit from the application of a chemical shift-based water-fat separation approach.

From an MR acquisition point of view, different techniques have been applied in the segmentation of the SAT and non-SAT regions both in the abdomen and the skeletal muscle. Water-fat imaging using a chemical shift-based approach is advantageous over water-fat imaging using a frequency selective excitation approach (12,14), as a chemical shift-based approach is insensitive to main magnetic field inhomogeneity effects. A chemical-shift based approach incorporating a multi-peak fat spectrum model (28,31) can also achieve a higher contrast between the water signal on the water image and the fat signal in the fat image than an approach based on water-fat selective excitation.

From an image analysis point of view, different techniques have been applied in the segmentation of the SAT and non-SAT regions. Specifically, previous studies have suggested the determination of the inner contour of the SAT region based on active contour models (10,14) and on the thresholding of the fat fraction map (21,37). The techniques employing active contours modeling require the empirical determination of additional parameters provided as input to the deformable model algorithm. The techniques employing thresholding of the fat fraction map are usually combined with operations imposing a convex shape for the SAT inner contour, as it would be necessary for example in fatty-degenerated thigh muscles with large regions of intermuscular fat between different muscles and next to the subcutaneous fat ring (i.e. thigh of female subject older than 50 years in Fig. 4). A determination of the SAT inner contour based on unsupervised clustering of water, fat and in-phase images and simple morphological operations, as proposed here, requires a minimum number of additional parameters (size of morphological operations) and can handle cases where there is a large intermuscular fat region next to the SAT inner contour.

Partial volume effects have been shown to have a strong impact on VAT measurements of lean subjects (11). Different techniques have been applied in distinguishing between adipose tissue and non-adipose tissue in voxels with partial volume effects, including applying a Gaussian mixture model on T_1-weighted images (10), k-means clustering on T_1-weighted water-suppressed and fat-suppressed images (14) and fuzzy clustering on T_1-weighted

images (13). Instead the measurement of fat volume in the proposed approach is based on the proton-density weighted fat fraction map from a chemical shift-based water-fat separation approach after the correction of multiple confounding factors (28,31–33). Computing the fat volumes based on the fat fraction map can considerably reduce partial volume effects especially when investigating small fat depots as the IMAT (19) and when investigating small fat volume changes in longitudinal studies.

An automatic segmentation approach for the calculation of SAT and muscle regions with low sensitivity to partial volume effects has also the tremendous advantage of reducing the total postprocessing time. The processing time of the automatic segmentation in comparison with the manual segmentation can be reduced enormously (i.e. 1000 times speed-up in the present implementation). This reduction of the post-processing time can be extremely beneficial in large-scale patient studies investigating changes in skeletal muscle fat volume and distribution.

The present study has some limitations. First, the computation of SAT and IMAT area (in single slice data) or volume (in multi-slice data) using the proton density fat fraction of the chemical shift-based water-fat separation neglects the proton contributions from other non-free-water and non-fat moieties with fast T_2 decay (i.e. macromolecules) (38–40). Computation of absolute fat area/volume would require an appropriate reference fat signal (41,42). Second, the automatic segmentation methodology was applied on single slice data. A single slice was selected per subject such that the derived group dataset spans the entire range of different degrees of fat infiltration, in order to test the performance of the proposed segmentation approach. A thorough comparison of the effect of single slice versus multi-slice processing on SAT and IMAT area calculation was outside the scope of the present study. However, the methodology could be easily applied to multi-slice data on a slice-by-slice fashion. Third, manual correction of the SAT and muscle region masks might be needed in certain extreme cases (as it is also shown in Fig. 8). The first case of Fig. 8 shows a slice of a subject with extreme fat infiltration of the MG muscle, where the automatic segmentation results in an underestimation in the IMAT area, as part of the IMAT was included in the SAT mask. The group calf data also showed that the accuracy in the subjects with high grade of fatty infiltration or high IMAT area was reduced relative to those with lower fatty infiltration grades or lower IMAT area in the calf. This occurs due to lack of image information in the definition of the SAT inner contour when an entire muscle next to the SAT region is completely fatty infiltrated or surrounded by a substantial amount of subfascial fat. Such cases would be also a problem for most of the other algorithms relying simply on signal intensity values. The second case of Fig. 8 shows a slice with very thin cortical bone, where the automatic segmentation results in an overestimation in the IMAT area, as the bone marrow within the tibia was included in the muscle region mask. The detection of very thin cortical bone has been also reported as a problem in automatic segmentation by Positano et al. (10) and could be potentially avoided by increasing the spatial resolution of the image acquisition. Another extreme case where manual correction of the SAT and muscle region masks might be necessary would be in subjects with very little SAT (i.e. patients with lipodystrophies).

The presented automatic segmentation approach could be further extended to address some of the above limitations. First, the morphological operations of the algorithm could be extended from 2D to 3D, after the incorporation of a coil correction step (i.e. N3 algorithm (43)) to address signal inhomogeneities due to coil profile effects in the slice direction. Second, texture features and edge information could be additionally extracted from the water and fat separated images to overcome the issue of misclassification in the SAT inner contour extraction for cases of completely fatty infiltrated muscles next to the subcutaneous fat ring. Third, the automated segmentation algorithm could be further improved by extending it

from an unsupervised classification model to a supervised method. Finally, the calf and thigh datasets used in the present study have been acquired using a phased-array knee coil and therefore show moderate in-plane signal intensity inhomogeneity due to coil profile effects. The observed moderate in-plane signal intensity inhomogeneity does not affect the performance of the employed k-means clustering approach. More severe in-plane signal intensity inhomogeneity should be expected in datasets acquired using phased-array surface coils, where application of the presented automatic segmentation approach should be preceded by an appropriate coil correction step (43).

The performance of the proposed automatic segmentation approach has been examined in the skeletal muscles of the lower extremities. Extensions of the proposed method to the skeletal muscles of the upper extremities should be straightforward. However, it would be necessary to combine the proposed method with additional processing steps for the extraction of bone marrow regions with intermediate fat fractions (i.e. vertebral bodies) (37) in order to extend the proposed technique to the abdomen.

In conclusion, the proposed multi-parametric segmentation method combined with a chemical shift-based water-fat separation approach accounting for multiple confounding factors in the quantification of fat fraction can provide an accurate and reliable automated calculation of the SAT and IMAT areas. The technique was validated in a range of cases in the calf and thigh muscle of young and elderly subjects, considerably reducing the total post-processing that a manual contouring approach would require for the extraction of SAT and IMAT areas.

Acknowledgments

Grant support: The present work was supported by the National Institutes of Health grants R01-AG17762 and RC1-AR058405.

References

1. Goodpaster BH, Thaete FL, Kelley DE. Thigh adipose tissue distribution is associated with insulin resistance in obesity and in type 2 diabetes mellitus. Am J Clin Nutr. 2000; 71(4):885–892. [PubMed: 10731493]
2. Wajchenberg BL. Subcutaneous and visceral adipose tissue: their relation to the metabolic syndrome. Endocr Rev. 2000; 21(6):697–738. [PubMed: 11133069]
3. Fox CS, Massaro JM, Hoffmann U, et al. Abdominal visceral and subcutaneous adipose tissue compartments: association with metabolic risk factors in the Framingham Heart Study. Circulation. 2007; 116(1):39–48. [PubMed: 17576866]
4. Boettcher M, Machann J, Stefan N, et al. Intermuscular adipose tissue (IMAT): association with other adipose tissue compartments and insulin sensitivity. J Magn Reson Imaging. 2009; 29(6): 1340–1345. [PubMed: 19422021]
5. Gallagher D, Kelley DE, Yim JE, et al. Adipose tissue distribution is different in type 2 diabetes. Am J Clin Nutr. 2009; 89(3):807–814. [PubMed: 19158213]
6. Gallagher D, Kuznia P, Heshka S, et al. Adipose tissue in muscle: a novel depot similar in size to visceral adipose tissue. Am J Clin Nutr. 2005; 81(4):903–910. [PubMed: 15817870]
7. Machann J, Thamer C, Schnoedt B, et al. Age and gender related effects on adipose tissue compartments of subjects with increased risk for type 2 diabetes: a whole body MRI/MRS study. Magma. 2005; 18(3):128–137. [PubMed: 16001284]
8. Machann J, Thamer C, Stefan N, et al. Follow-up whole-body assessment of adipose tissue compartments during a lifestyle intervention in a large cohort at increased risk for type 2 diabetes. Radiology. 2010; 257(2):353–363. [PubMed: 20713612]

9. Mojtahedi MC, Thorpe MP, Karampinos DC, et al. The effects of a higher protein intake during energy restriction on changes in body composition and physical function in older women. J Gerontol A Biol Sci Med Sci. 2011; 66:1218–1225. [PubMed: 21798863]
10. Positano V, Christiansen T, Santarelli MF, Ringgaard S, Landini L, Gastaldelli A. Accurate segmentation of subcutaneous and intermuscular adipose tissue from MR images of the thigh. J Magn Reson Imaging. 2009; 29(3):677–684. [PubMed: 19243051]
11. Zhou A, Murillo H, Peng Q. Impact of partial volume effects on visceral adipose tissue quantification using MRI. J Magn Reson Imaging. 2011; 34(6):1452–1457. [PubMed: 21964770]
12. Zhou A, Murillo H, Cusi K, Peng Q. Comparison of visceral adipose tissue quantification on water suppressed and nonwater-suppressed MRI at 3.0 tesla. J Magn Reson Imaging. 201210.1002/jmri.23582
13. Zhou A, Murillo H, Peng Q. Novel segmentation method for abdominal fat quantification by MRI. J Magn Reson Imaging. 2011; 34(4):852–860. [PubMed: 21769972]
14. Makrogiannis S, Serai S, Fishbein KW, Schreiber C, Ferrucci L, Spencer RG. Automated quantification of muscle and fat in the thigh from water-, fat-, and nonsuppressed MR images. J Magn Reson Imaging. 2012; 35(5):1152–1161. [PubMed: 22170747]
15. Dixon WT. Simple proton spectroscopic imaging. Radiology. 1984; 153(1):189–194. [PubMed: 6089263]
16. Glover GH, Schneider E. Three-point Dixon technique for true water/fat decomposition with B_0 inhomogeneity correction. Magn Reson Med. 1991; 18(2):371–383. [PubMed: 2046518]
17. Reeder SB, Pineda AR, Wen Z, et al. Iterative decomposition of water and fat with echo asymmetry and least-squares estimation (IDEAL): application with fast spin-echo imaging. Magn Reson Med. 2005; 54(3):636–644. [PubMed: 16092103]
18. Reeder SB, Wen Z, Yu H, et al. Multicoil Dixon chemical species separation with an iterative least-squares estimation method. Magn Reson Med. 2004; 51(1):35–45. [PubMed: 14705043]
19. Karampinos DC, Baum T, Nardo L, et al. Characterization of the regional distribution of skeletal muscle adipose tissue in type 2 diabetes using chemical shift-based water/fat separation. J Magn Reson Imaging. 2012; 35(4):899–907. [PubMed: 22127958]
20. Alabousi A, Al-Attar S, Joy TR, Hegele RA, McKenzie CA. Evaluation of adipose tissue volume quantification with IDEAL fat-water separation. J Magn Reson Imaging. 2011; 34(2):474–479. [PubMed: 21780238]
21. Kullberg J, Karlsson AK, Stokland E, Svensson PA, Dahlgren J. Adipose tissue distribution in children: automated quantification using water and fat MRI. J Magn Reson Imaging. 2010; 32(1):204–210. [PubMed: 20575078]
22. Alizai H, Nardo L, Karampinos DC, et al. Comparison of clinical semi-quantitative assessment of muscle fat infiltration with quantitative assessment using chemical shift-based water/fat separation in MR studies of the calf of post-menopausal women. Eur Radiol. 201210.1007/s00330-012-2404-7
23. Altman R, Asch E, Bloch D, et al. Development of criteria for the classification and reporting of osteoarthritis. Classification of osteoarthritis of the knee. Diagnostic and Therapeutic Criteria Committee of the American Rheumatism Association. Arthritis Rheum. 1986; 29(8):1039–1049. [PubMed: 3741515]
24. Li X, Benjamin Ma C, Link TM, et al. In vivo T(1rho) and T(2) mapping of articular cartilage in osteoarthritis of the knee using 3 T MRI. Osteoarthritis Cartilage. 2007; 15(7):789–797. [PubMed: 17307365]
25. Bolbos RI, Zuo J, Banerjee S, et al. Relationship between trabecular bone structure and articular cartilage morphology and relaxation times in early OA of the knee joint using parallel MRI at 3 T. Osteoarthritis Cartilage. 2008; 16(10):1150–1159. [PubMed: 18387828]
26. Beattie KA, MacIntyre NJ, Ramadan K, Inglis D, Maly MR. Longitudinal changes in intermuscular fat volume and quadriceps muscle volume in the thighs of women with knee osteoarthritis. Arthritis Care Res (Hoboken). 64(1):22–29. [PubMed: 21905259]
27. Yu H, Reeder SB, Shimakawa A, Brittain JH, Pelc NJ. Field map estimation with a region growing scheme for iterative 3-point water-fat decomposition. Magn Reson Med. 2005; 54(4):1032–1039. [PubMed: 16142718]

28. Yu H, Shimakawa A, McKenzie CA, Brodsky E, Brittain JH, Reeder SB. Multiecho water-fat separation and simultaneous R_2* estimation with multifrequency fat spectrum modeling. Magn Reson Med. 2008; 60(5):1122–1134. [PubMed: 18956464]
29. Middleton, MS.; Hamilton, G.; Bydder, M.; Sirlin, CB. How much fat is under the water peak in liver fat MR spectroscopy?. Proceedings of the 17th Annual Meeting of ISMRM; Honolulu, Hawaii. 2009. p. 4331
30. Karampinos DC, Yu H, Shimakawa A, Link TM, Majumdar S. Chemical shift-based water/fat separation in the presence of susceptibility-induced fat resonance shift. Magn Reson Med. 201210.1002/mrm.24157
31. Bydder M, Yokoo T, Hamilton G, et al. Relaxation effects in the quantification of fat using gradient echo imaging. Magn Reson Imaging. 2008; 26(3):347–359. [PubMed: 18093781]
32. Karampinos DC, Yu H, Shimakawa A, Link TM, Majumdar S. T(1) -corrected fat quantification using chemical shift-based water/fat separation: Application to skeletal muscle. Magn Reson Med. 2011; 66:1312–1326. [PubMed: 21452279]
33. Liu CY, McKenzie CA, Yu H, Brittain JH, Reeder SB. Fat quantification with IDEAL gradient echo imaging: correction of bias from T_1 and noise. Magn Reson Med. 2007; 58(2):354–364. [PubMed: 17654578]
34. Yu H, Shimakawa A, Hines CD, et al. Combination of complex-based and magnitude-based multiecho water-fat separation for accurate quantification of fat-fraction. Magn Reson Med. 2011; 66(1):199–206. [PubMed: 21695724]
35. Dice L. Measures of the amount of ecologic association between species. Ecology. 1945; 26:297–302.
36. Goutallier D, Postel JM, Bernageau J, Lavau L, Voisin MC. Fatty muscle degeneration in cuff ruptures. Pre- and postoperative evaluation by CT scan. Clin Orthop Relat Res. 1994; (304):78–83. [PubMed: 8020238]
37. Addeman, BT.; Beaton, M.; Hegele, RA.; Soliman, AS.; Wiens, CN.; McKenzie, CA. Validation of fully automatic adipose tissue segmentation and volume quantification. Proceedings of the 20th Annual Meeting of ISMRM; Melbourne, Australia. 2012. p. 751
38. Hu HH, Nagy TR, Goran MI, Nayak KS. Quantification of absolute fat mass by magnetic resonance imaging: a validation study against chemical analysis. Int J Body Compos Res. 2011; 9(3):111–122. [PubMed: 23204926]
39. Reeder, SB.; Hines, CD.; Yu, H.; McKenzie, CA.; Brittain, JH. On the definition of fat-fraction for *in vivo* fat quantification with magnetic resonance imaging. Proceedings of the 17th Annual Meeting of ISMRM; Honolulu, Hawaii. 2009. p. 211
40. Reeder, SB.; Hines, CD.; Yu, H.; McKenzie, CA.; Brittain, JH. Relationship between proton-density fat fraction and true fat concentration for in vivo fat quantification with magnetic resonance imaging. Proceedings of the 19th Annual Meeting of ISMRM; Montreal, Canada. 2011. p. 805
41. Cui, Y.; Yang, IY.; Wade, T.; Wiens, CN.; Soliman, AS.; McKenzie, CA. Absolute quantification of in vivo water and fat content. Proceedings of the 20th Annual Meeting of ISMRM; Melbourne, Australia. 2012. p. 363
42. Hu HH, Nayak KS. Quantification of absolute fat mass using an adipose tissue reference signal model. J Magn Reson Imaging. 2008; 28(6):1483–1491. [PubMed: 19025936]
43. Folkesson J, Krug R, Goldenstein J, et al. Evaluation of correction methods for coil-induced intensity inhomogeneities and their influence on trabecular bone structure parameters from MR images. Med Phys. 2009; 36(4):1267–1274. [PubMed: 19472635]

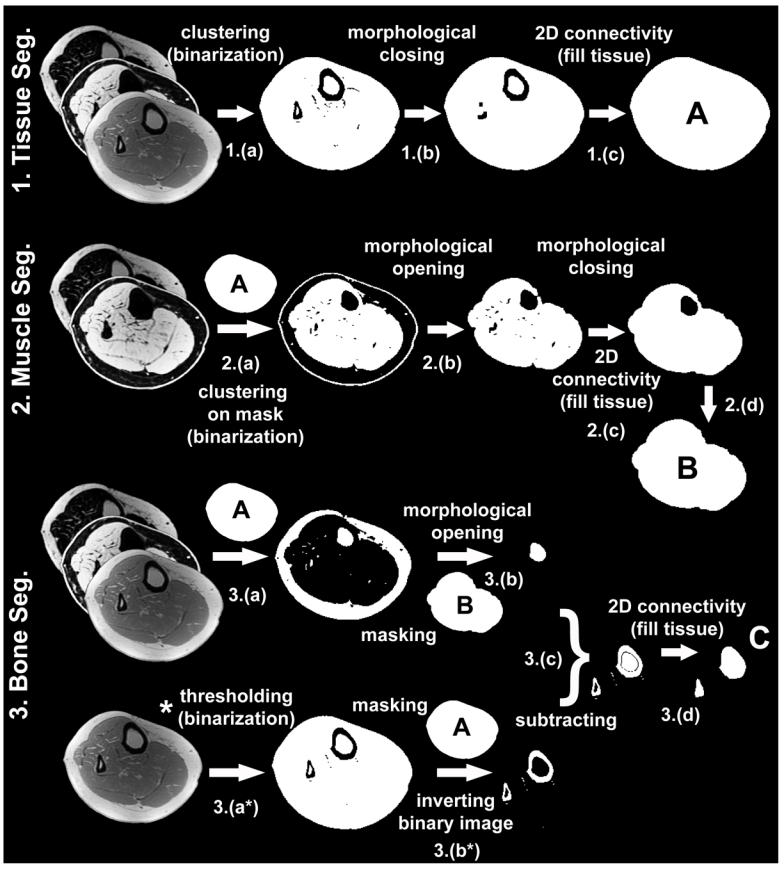

Figure 1.

Diagram of the segmentation algorithm for extracting the muscle and fat depot compartments via unsupervised clustering in order to quantify SAT and IMAT regions. In the first stage (stage 1), the tissues (calf or muscle) outer surface was determined (mask A). In the next stage (stage 2), the muscle region was detected, which defines the boundary between the SAT and IMAT regions (mask B). In the final stage (stage 3), the bones were detected (mask C).

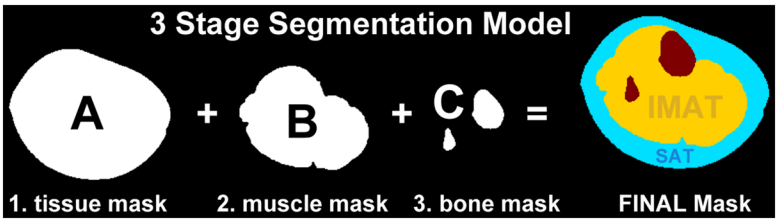

Figure 2.
Diagram of the definition of SAT and muscle regions based on the combination of the masks from the three segmentation stages (masks A, B and C).

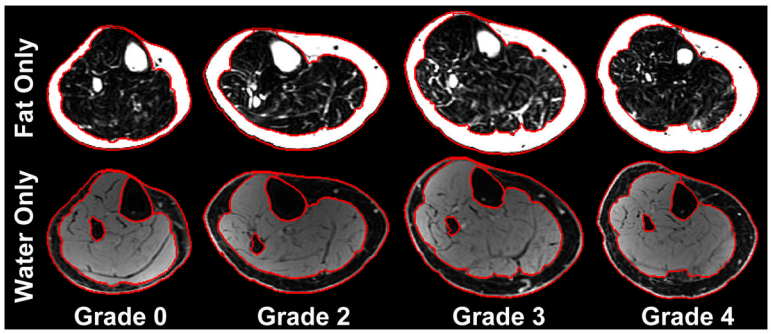

Figure 3.
Representative results of the multi-parametric segmentation for the SAT region mask (superimposed on the fat and water image) and muscle region mask (superimposed on the water image) in the calf of subjects with different grades of muscle infiltration in the medial gastrocnemius (MG). The grading is based on the semi-quantitative Goutallier scoring method.

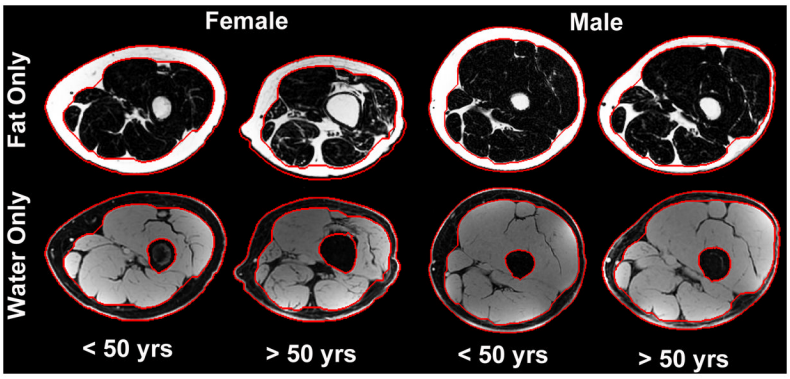

Figure 4.
Representative results of the multi-parametric segmentation for the SAT region (superimposed on the fat and water image) and muscle region (superimposed on the water image) in the thigh of two male and two female subjects with different ages.

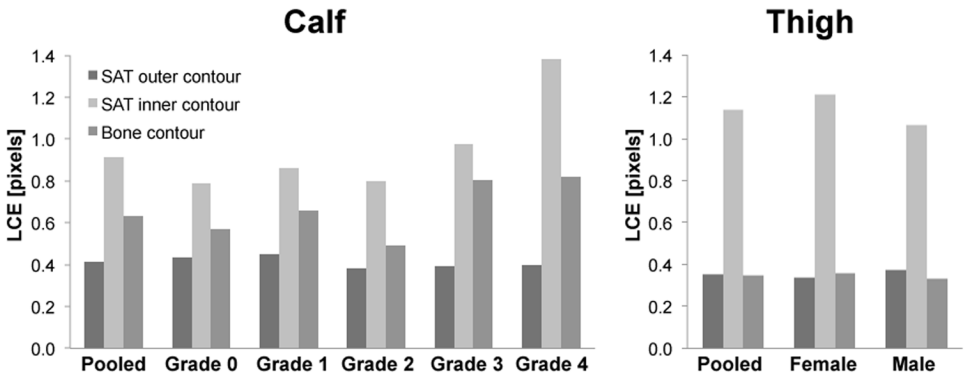

Figure 5.

The local contouring error (LCE) in pixels for the SAT outer and inner contour, and bone contour compared to the GT for both tissues (thigh and calf); (a) the LCE in the calf for all contours are shown for female and male (b) different muscle infiltration grades (G0 – G4) are used for validation the automatic approach in the calf (e.g. LCE).

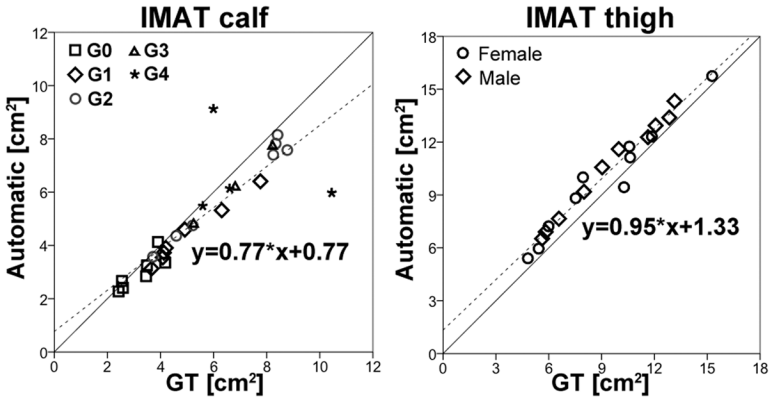

Figure 6.

Regression analysis results for the agreement in IMAT areas between manual segmentation (ground truth-GT) and automatic segmentation in the calf and thigh data. Solid line represents the identity line and dashed line represents the derived regression line.

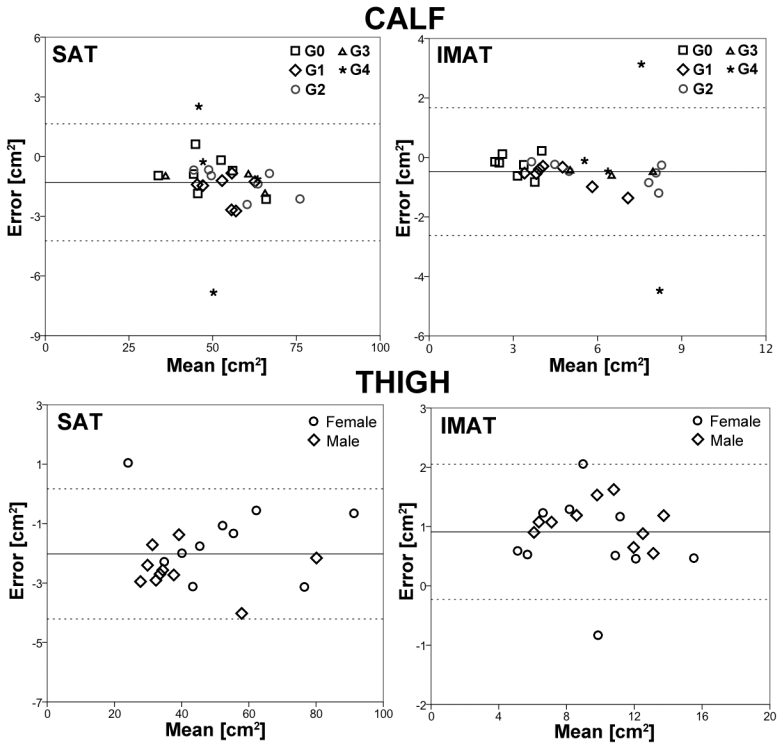

Figure 7.

Bland-Altman plots comparing SAT and IMAT areas calculated using the automatic segmentation versus the ground truth (GT) in the calf and the thigh. The plots provide estimates of systematic and random errors. Dotted lines on the Bland-Altman plots represent 95% confidence intervals for agreement between the automatic approach and the manual contouring as GT.

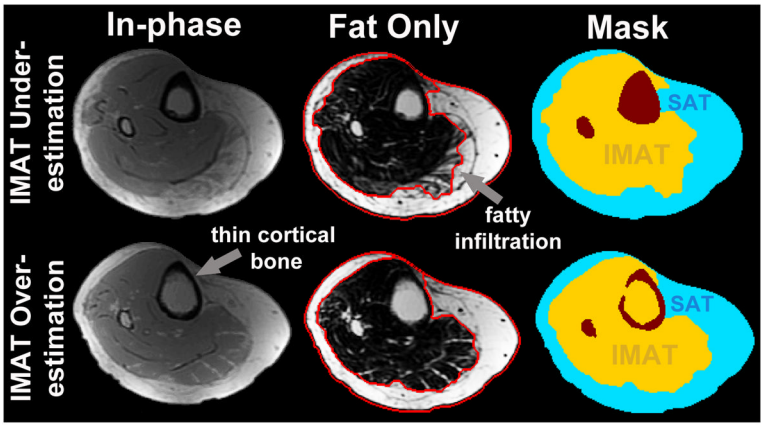

Figure 8.

Extreme cases where automatic segmentation leads to IMAT area underestimation or overestimation compared to the manual segmentation. The inability to accurately detect the SAT inner contour next to highly fatty infiltrated muscles can lead to an underestimation of IMAT area. The inability to entirely detect bones (i.e. fibula and tibia) due to thin cortical bones can lead to an overestimation of the IMAT area.

Table 1

Linear regression results for the agreement of SAT and IMAT area estimates between the automatic segmentation approach and manual contouring (ground truth) in the calf and the thigh.

Measurement	Tissue	Parameter	Estimate	P-value	R2
SAT	calf	Slope	0.955 ± 0.130	0.130	0.98
		Intercept	1.142 ± 0.468	0.468	
IMAT	calf	Slope	0.774 ± 0.024	0.024[a]	0.75
		Intercept	0.771 ± 0.163	0.163	
SAT	thigh	Slope	1.043 ± 0.145	0.145	0.98
		Intercept	−7.479 ± 0.721	0.721	
IMAT	thigh	Slope	0.954 ± 0.327	0.327	0.96
		Intercept	1.335 ± 0.010	0.010[b]	

Significance is determined from a two-tailed Student's t-test with null hypothesis slope =1 and intercept = 0

[a] Slope is significantly different from one (α =0.05)

[b] Intercept is significantly different from zero (α = 0.05)